Materials Horizons

ROYAL SOCIETY OF CHEMISTRY

COMMUNICATION

View Article Online
View Journal | View Issue

Check for updates

Cite this: *Mater. Horiz.*, 2021, 8, 3149

Received 11th June 2021,
Accepted 23rd September 2021

DOI: 10.1039/d1mh00919b

rsc.li/materials-horizons

Charge trapping with α-Fe_2O_3 nanoparticles accompanied by human hair towards an enriched triboelectric series and a sustainable circular bioeconomy†

Ishita Chakraborty,[a] Sz-Nian Lai,[b] Ming-Chung Wu,[cde] Hsun-Yen Lin,[b] Chuan Li,[f] Jyh Ming Wu *[bg] and Chao-Sung Lai *[ahij]

This work reports a new approach to amending polydimethylsiloxane (PDMS) by supporting α-Fe_2O_3 nanoparticles (NPs), thereby generating a material suitable for use as a negative triboelectric material. Additionally, human hair exhibits a profound triboelectrification effect and is a natural regenerative substance, and it was processed into a film to be used as a positive triboelectric material. Spatial distribution of α-Fe_2O_3 NPs, the special surface morphologies of a negative tribological layer containing nano-clefts with controlled sizes and a valley featuring a positive tribolayer based on human hair made it possible to demonstrate facile and scalable fabrication of a triboelectric nanogenerator (TENG) presenting enhanced performance; this nanogenerator produced a mean peak-to-peak voltage of 370.8 V and a mean output power density of 247.2 μW cm^{-2} in the vertical contact-separation mode. This study elucidates the fundamental charge transfer mechanism governing the triboelectrification efficiency and its use in harvesting electricity for the further development of powerful TENGs suitable for integration into wearable electronics and self-charging power cells, and the work also illustrates a recycling bioeconomy featuring systematic utilization of human hair waste as a regenerative resource for nature and society.

New concepts

We pioneer the utilization of the novel properties of hematite (α-Fe_2O_3) nanoparticles into a triboelectric nanogenerator (TENG) by embedding them in a polydimethylsiloxane matrix to develop a negative triboelectric layer accompanied by a human hair based film as the positive triboelectric layer. Although, human hair is considered to be a highly triboelectric material, it is a great challenge to process it into a form useful for incorporating into practical triboelectric nanogenerator devices, demonstrating stable output performance. Significant research has been conducted to improve the low output of TENGs incorporating pure PDMS, but there are still several drawbacks, like the thickness of the porous PDMS film introducing difficulty to meet the requirements of small size and light weight for wearable applications and expansion of the maintenance time due to increased thickness. We have overcome these limitations by fabricating a light weight, flexible and high-performance bio-based TENG consisting of PDMS@α-Fe_2O_3 NP composite thin film enhancing the charge trapping of induced tribo charges through the electret doping effect resulting from the dielectric properties of the hematite nanoparticles and processed the bio-waste human hair into a convenient positive electrification layer to initiate a systematic approach towards a circular bio-economy for the sake of society and the environment.

Introduction

The burgeoning of multifunctional electronic devices is one of the important reasons to seek feasible technologies capable of harvesting energy from the surrounding environment. Nature provides abundant sources of energy such as solar, wind, water, and mechanical energy; if utilized, these sources would constitute a partial solution to the limited supply of fossil fuels and the resulting energy crisis. Since 2012, the triboelectric nanogenerator (TENG) has provided new possibilities for converting small amounts of mechanical energy into electrical energy based on the coupling of triboelectrification and electrostatic induction,[1] and it has been proven to be a cost-effective,[2] simple, and efficient technique for generating a high power density from the environment.[3,4]

[a] *Department of Electronic Engineering, Chang Gung University, Taoyuan, Taiwan. E-mail: cslai@mail.cgu.edu.tw*
[b] *Department of Materials Science and Engineering, National Tsing Hua University, Hsinchu, Taiwan. E-mail: wujm@mx.nthu.edu.tw*
[c] *Department of Chemical and Materials Engineering, Chang Gung University, Taoyuan, Taiwan*
[d] *Green Technology Research Center, Chang Gung University, Taoyuan, Taiwan*
[e] *Division of Neonatology, Department of Pediatrics, Chang Gung Memorial Hospital, Taoyuan, Taiwan*
[f] *Department of Biomedical Engineering, National Yang Ming Chiao Tung University, Taipei, Taiwan*
[g] *High Entropy Materials Center, National Tsing Hua University, Hsinchu, Taiwan*
[h] *Department of Nephrology, Chang Gung Memorial Hospital, Taoyuan, Taiwan*
[i] *Department of Materials Engineering, Ming-Chi University of Technology, New Taipei City, Taiwan*
[j] *Artificial Intelligent Innovation Research Center, Chang Gung University, Taoyuan, Taiwan*

† Electronic supplementary information (ESI) available. See DOI: 10.1039/d1mh00919b

In essence, contact between two electrification layers generates triboelectric charges with opposite polarities on the two surfaces, and these induced triboelectric charges flow back and forth through an external circuit during repeated contact and release movements.[5] The main factors influencing TENG performance include the surface morphology, dielectric constant and triboelectric potential difference between the two triboelectric layers.[6,7] In conventional TENGs, the two electrification layer materials are chosen to have a large difference in surface potential, *e.g.*, with a polymer material (*i.e.*, Teflon)[8] terminated with the most electronegative functional group functioning as the negative side and a low work function material (*i.e.*, Al metal)[9] serving as the positive side. Polydimethylsiloxane (PDMS) is the second most negative material in the triboelectric series, after poly-(tetrafluoroethylene) (PTFE), but PDMS is in higher demand as a negative triboelectric material because of its flexibility, transparency, ability to mix with numerous nanostructured materials to form various composite films, ability to coat other surfaces and, very importantly, hydrophobic surface, which makes the electrical output of the TENGs less sensitive to the moisture in the air.[10] While many promising materials are available as the negative electrification layer in the triboelectric series, only a few materials are recognized as the positive electrification layer that can be incorporated into practical devices, so further expansion of this series is required.[8,11]

The use of TENGs as promising energy harvesters in practical applications necessitates the reasonable design of triboelectric materials that induce a high surface charge density by offering a very high physical contact area between the triboelectric layers, while also maintaining a simple fabrication procedure. Despite the substantial advantages of PDMS, the very small output current and low output voltage of TENGs incorporating pure PDMS limit their practical application for electronic devices. Many studies have illustrated significant improvement in the output performance of TENGs by using different strategies to control the surface morphology or effect interior structural modification of PDMS films; these strategies include surface patterning,[12] addition of chemical functional groups by using block copolymers,[13] treatment of PDMS with fluorocarbons,[14] or plasma etching,[14] all of which typically involve high cost. Consequently, the need to find a simple and cost-effective approach to preparing high-performance TENGs has been widely accepted. Recently, impressively high outputs have been generated from PDMS-based TENGs by forming porous sponge structures or adding nanostructured materials[15,16] to take advantage of the large surface area-to-volume ratios and high dielectric constants. Although these two methods offer considerable improvement in the outputs of TENGs, there are still several shortcomings; for example, the thickness of the porous PDMS film makes it difficult to meet the requirements of small size and light weight for a wearable device, and an increase in thickness would expand the cleaning time, which would deteriorate the characteristics of PDMS. Human skin and hair exhibit very high positive tribo-polarity, and various publications have reported TENGs based on human skin.[11,17] However, because of the difficulty of processing hair into a convenient and consistent form for inclusion in practical devices, there is only one study demonstrating the use of human hair to fabricate TENGs;[18] this TENG suffered from a lack of output stability, although it exhibited appreciably high output. Therefore, a low cost method providing appreciably high power density, simple processing, light weight, and limited environmental impact is urgently needed.

A significant amount of research has been focused on different metal oxides because of their extremely high specific capacitance values, but the limitations of most of these metal oxides arise from their toxicity, cost and limited availability. Among all semiconductor nanomaterials, hematite (α-Fe_2O_3), an n-type semiconductor (E_g = 2.1 eV), is the most thermodynamically stable iron oxide, and its low cost, ready availability, environmental friendliness and corrosion resistance make it a promising candidate for applications involving rechargeable electrodes, batteries,[19] supercapacitors,[20] gas sensors,[21] photocatalysts,[22] magnetic resonance imaging systems,[23] *etc.* In this study, we describe the first discovery of a high output TENG, which was designed by using the novel properties of hematite (α-Fe_2O_3) nanoparticles embedded in a PDMS matrix in the negative triboelectrification layer. We report a simple, efficient and rapid approach to fabricating high-performance TENGs by using a composite poly-(dimethylsiloxane) (PDMS) film with embedded α-Fe_2O_3 nanoparticles (NPs) as the negative triboelectrification layer and human hair as a positive triboelectrification layer. The effect of α-Fe_2O_3 NP incorporation into the PDMS matrix and the use of a human hair-based positive electrification layer on the performance of the TENG were also investigated with a comparative study. The α-Fe_2O_3 NPs embedded in PDMS films acted as charge-trapping sites capable of increasing the relative dielectric property of the films and resulted in TENG output considerably higher than that of a pure PDMS film. The use of human hair permits the fabrication of cost-effective TENGs and alleviates a challenge to waste management systems, since human hair is a rapidly growing natural resource but a slowly degrading waste material without a closed-loop system for recovery and regeneration, which makes it environmentally harmful yet also valuable. Therefore, there is a huge opportunity to utilize hair waste found in municipal waste streams around the world and turn it into something beneficial for both the economy and the environment. As presented in Fig. 1, by using this novel combination of a PDMS@α-Fe_2O_3 NP composite as the negative electrification layer and a human hair-based positive electrification layer, a high-performing TENG has been developed as a promising green energy source for the recycling economy, thereby eliminating waste and promoting a closed-loop system that minimizes the use of resource inputs.

Results and discussion

Fig. 2a shows FE-SEM images of the as-synthesized PDMS@α-Fe_2O_3 NP composite with 0.06 wt% α-Fe_2O_3 NPs. As shown in

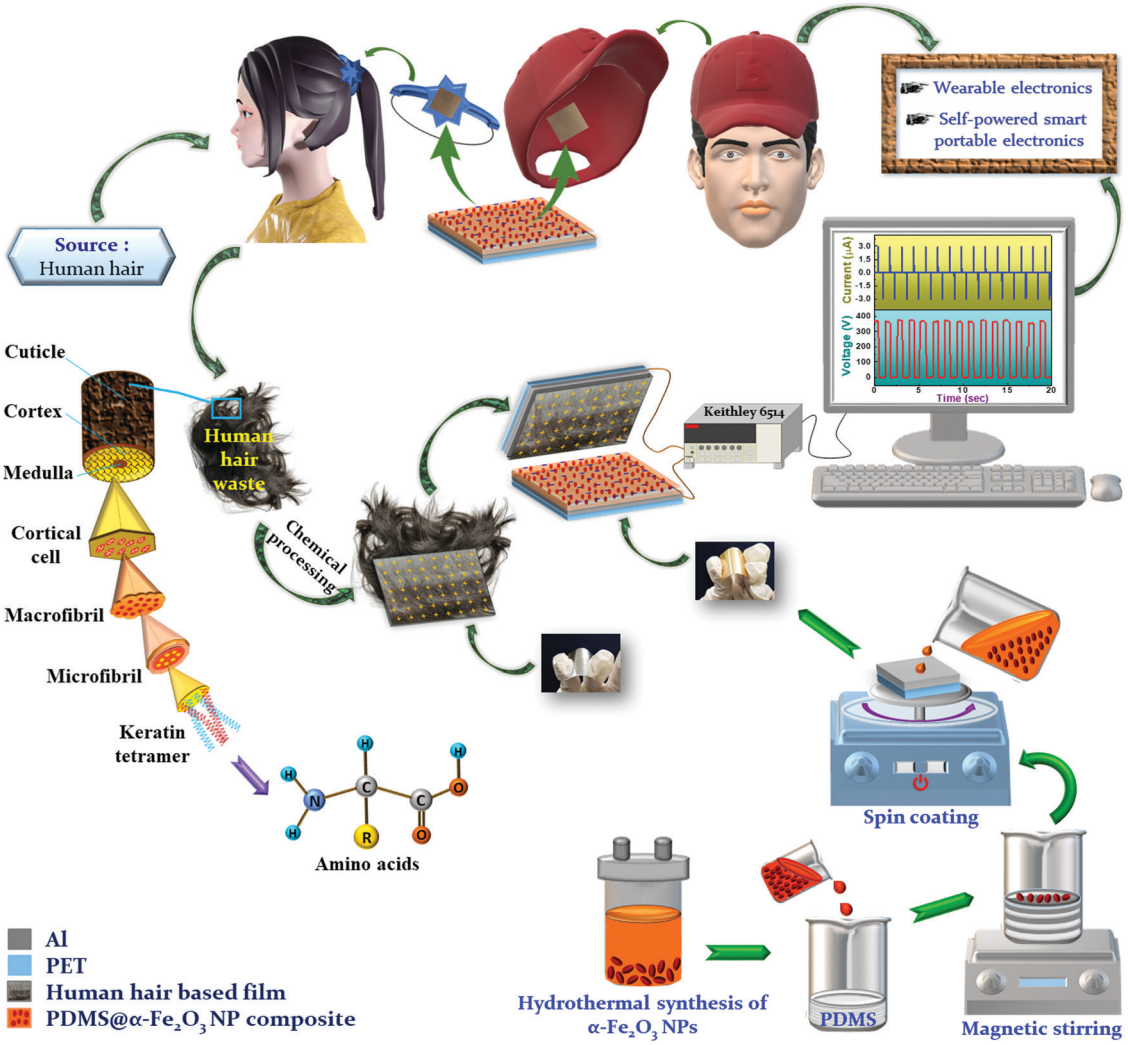

Fig. 1 Human hair as a recycled material: adding value to the circular bioeconomy with waste protein fibers through effective TENG-based mechanical-to-electrical signal conversion technology.

Fig. S2a (ESI†), the as-synthesized α-Fe_2O_3 NPs exhibited a nanorod-like morphology with 50 nm widths and 150–200 nm lengths. The pure PDMS film (Fig. S2b, ESI†) showed a flat surface morphology without considerable surface modifications, but all composite samples (Fig. 2a and Fig. S2c–e, ESI†) showed a rough and dry arable land-like morphology, which was due to the presence of irregular nano-clefts resulting from increased surface tension caused by evaporation of DI water from the PDMS@α-Fe_2O_3 NP composite film during drying. With increasing NP content in the composite, the DI water content also increased, so evaporation caused the dimensions of the nano-clefts to increase from 1–2 nm to 30–50 nm. In comparing PF_1 (Fig. S2c, ESI†) to PF_2 (Fig. 2a), the change in film morphology with an increase in the nanosized clefts may have a positive influence on the TENG performance; with a further increase in NPs, however, the nano-cleft began causing detachment within the electrification layer, which caused degradation of the composite film. As shown in Fig. S2c (ESI†) for PF_1, although there were less α-Fe_2O_3 NPs in the PDMS matrix, they were agglomerated, which may be due to an insufficient amount of solvent in relation to the amount of PDMS used. Additionally, α-Fe_2O_3 NPs were nearly covered by the PDMS film, which altered their influence on TENG performance. In the case of PF_2 (Fig. 2a), α-Fe_2O_3 NPs were almost uniformly distributed in the PDMS matrix without agglomeration, and they were suitably embedded, which improved the mechanical strength of the film.[9] Thus, despite the presence of nano clefts, the film does not suffer considerable detachment and shows noticeably enhanced TENG performance.

In the case of PF_3 and PF_4 (Fig. S2d and e, ESI†), agglomeration of the α-Fe_2O_3 NPs led to detachment caused by the increased dimensionality of the nano-clefts, degradation in mechanical strength within the composite film and the loss of surface features; all of these factors led to the deterioration of TENG performance. The probability of aggregation by the α-Fe_2O_3 NPs increased as the NP content increased because we have not used surfactant to disperse the NPs in the PDMS solutions. Obviously, the effective friction area of PDMS (high

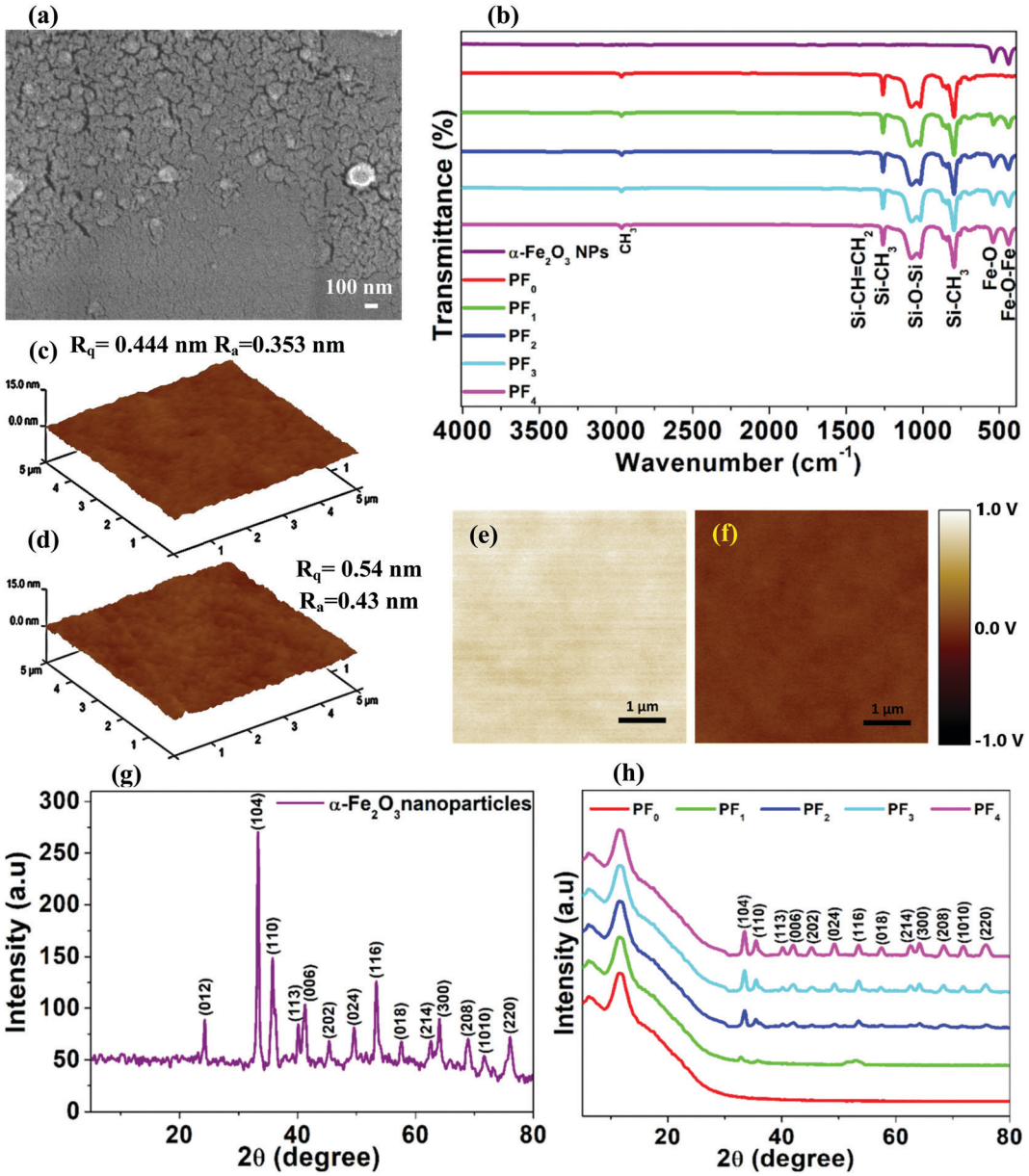

Fig. 2 (a) FESEM view of the PF_2 film and (b) FTIR spectra of α-Fe_2O_3 NPs, PDMS, and PDMS@α-Fe_2O_3 NP composites; AFM images (three-dimensional) of the (c) PDMS film and (d) PF_2 film; KPFM images of (e) PDMS film and (f) PF_2 film. XRD plots of (g) α-Fe_2O_3 nanoparticles and (h) PDMS@α-Fe_2O_3 NP composites.

negative electricity) decreased with increasing amounts of α-Fe_2O_3 NPs because the nanoparticles began to appear on the surface at higher filling levels. As shown by the energy-dispersive X-ray spectroscopy (EDS) spectra for PDMS, α-Fe_2O_3 NPs and PF_2 (Fig. S3, ESI†), Fe, O, C, and Si are present at levels of 5.56, 31.92, 49, and 13.52%, respectively (Table 1), due to the successful incorporation of α-Fe_2O_3 NPs into the PDMS matrix.

XRD was used to investigate the crystal structures of the as-prepared samples. Fig. 2h shows a plot of the diffraction patterns for PDMS and the PDMS@α-Fe_2O_3 NP composites to allow comparison of the peaks. The XRD pattern (Fig. 2g) of the as-grown α-Fe_2O_3 NPs was consistent with those in previous reports,[19,20] and the crystallinity in the nanocomposite film was

Table 1 EDS analysis of the PDMS films, α-Fe_2O_3 NPs and PDMS@α-Fe_2O_3 NP composite with 0.06 wt% α-Fe_2O_3 NPs

Elements	Samples	PDMS	α-Fe_2O_3 NPs	PDMS@α-Fe_2O_3 NP
C K	Weight%	45.15	0	48.56
	Atomic%	44.21	0	49
O K	Weight%	38.22	65.14	30.89
	Atomic%	38.56	64.03	31.92
Si K	Weight%	16.63	0	14.25
	Atomic%	17.23	0	13.52
Fe L	Weight%	0	34.86	6.30
	Atomic%	0	35.97	5.56

maintained without introducing any change in the PDMS standard XRD profile. The amorphous halo at $2\theta = 12^\circ$ was typical of the XRD pattern of PDMS, indicating that the addition of α-Fe_2O_3 NPs did not increase the crystalline domain of the films. The XRD patterns of α-Fe_2O_3 were well matched with the standard diffraction peaks (JCPDS card no. 33-0664), and the absence of additional peaks confirmed the formation of the pure hematite phase. As the α-Fe_2O_3 NP content increased, diffraction peaks for α-Fe_2O_3 gradually developed, indicating an increase in the amount of incorporated α-Fe_2O_3 NPs. The XRD patterns also confirmed the introduction of pure α-Fe_2O_3 into the PDMS matrix with almost no change in chemical composition.

FTIR provides an approach to identifying compounds or the purity of materials, and infrared radiation in the range 4000 to 400 cm^{-1} is used to irradiate the sample. The FTIR spectra of the pristine PDMS film, pure α-Fe_2O_3 NP and PDMS@α-Fe_2O_3 NP composites are shown in Fig. 2b. The typical peak at approximately 2965 cm^{-1} represented the C–H methyl stretch, and the silicon–methyl bond was responsible for the band at 1260 cm^{-1}. In addition, the broad absorption band between 1130 and 1000 cm^{-1} for the polymer backbone was identified.[24] The amount of unreacted vinyl and hydrosilane (SiH) groups (after cross-linking) can be determined by the intensity of the absorption bands at 1410 cm^{-1} and 2140 cm^{-1}, respectively.[24] In our present study, the intensity of the absorption band at 1410 cm^{-1} was low, and no absorption band was observed at 2140 cm^{-1}, indicating the presence of very few unreacted vinyl groups and no excess hydrosilane (SiH) groups.[24] The characteristic peaks at approximately 540 cm^{-1} and 432 cm^{-1} corresponded to bonds in α-Fe_2O_3,[25] which are absent in the pure PDMS sample but become more intense due to the insertion of an increasing amount of α-Fe_2O_3 NPs into the PDMS matrix in forming PDMS@α-Fe_2O_3 NP composites.

To investigate the effect of inserting α-Fe_2O_3 NPs into the PDMS matrix, the average roughness and the surface potentials of the PDMS and PDMS@α-Fe_2O_3 NP composite films were characterized using atomic force microscopy (AFM) and Kelvin probe force microscopy (KPFM). From the AFM images (Fig. 2c and d and Fig. S5b–d, ESI†) and Table S1 (ESI†), the root mean square (rms) roughness of the PDMS@α-Fe_2O_3 NP composite film surface was found to increase with an increase in NP content, featuring the formation of nano-clefts. These clefts were caused by stress relaxation due to curing and subsequent cooling of spin-coated PDMS films.[26] Furthermore, the increase in the amount of DI water in solutions of NPs, along with the longer curing time, caused an increase in the number of surface nano-clefts; this resulted in high surface roughness that effectively increased the surface area. Interestingly, the addition of very small amounts of α-Fe_2O_3 NPs into the PDMS matrix shifted the relative surface charge potential toward lower values compared with those obtained from pristine PDMS, as depicted by the KPFM images (Fig. 2e and f and Fig. S6, ESI†). This significant drop in the surface charge potential of the PDMS@α-Fe_2O_3 NP composite film was expected to increase the difference in triboelectric potentials for the top and bottom electrification layers; the film should exhibit much stronger ability to accept electrons when in contact with the same positive triboelectric layer, which would thereby enhance TENG performance.[27] The insertion of α-Fe_2O_3 NPs in amounts exceeding 0.06 wt% increased the surface potential and reduced the triboelectric potential difference with the human hair-based film; this was ascribable to α-Fe_2O_3 NP agglomeration and detachment within the negative electrification layer, which caused degradation of the composite film and affected the outputs of the TENGs.[28]

Morphological and chemical investigation of the human hair film was carried out by FE-SEM and energy-dispersive X-ray spectroscopy (EDS). The surface morphology of the film is shown in Fig. 3a, and it exhibits a surface valley feature with complete coverage over the Al electrode; the surface roughness was enhanced (ESI,† Fig. S5a and Fig. 3b), even without any vestige of undissolved hair, thus improving its performance as a positive electrification layer.

Fig. S4 (ESI†) and Table 2 show the EDS spectra and the weight and atomic percentages of each element in the as-prepared human hair film. Usually, the main chemical elements present in hair are carbon (45%), oxygen (28%), nitrogen (15%), hydrogen (6.7%), sulfur (5.3%) and trace various elements, including Ca, Mg, Sr, B, Al, Si, Na, K, Zn, Cu, Mn, Fe, Ag, Au, Hg, As, Pb, Sd, Ti, W, Mo, I, P, and Se. All chemical concentrations we determined for the human hair-based electrification layer were comparable to the usual amounts found in human hair.[29] We obtained similar EDS analysis results from the dark and bright shaded regions in the FE-SEM images (Fig. 3a and Fig. S2f, ESI†), which confirms that the valley surface featured a film with complete coverage over the Al electrode.

To analyze the FTIR data (Fig. 3c) for the human hair-based film from high to low wavenumbers, a broad peak appeared at approximately 3080–3557 cm^{-1}, which may be due to asymmetric and symmetric H–O–H stretching, amide A (N–H stretch in resonance with amide II overtone) and amide B bands.[30] The peak at approximately 2965 cm^{-1} resulted from the asymmetric stretching mode of CH_3.[18,30] The peak at approximately 1600–1700 represented Amide I bands, mainly the bands of the β region of the pleated structure conformation of proteins, and the C═C stretching mode;[31] the peak at 1645 cm^{-1} arose from H–O–H bending,[30] so the very sharp peak at 1637 cm^{-1} most likely originated from overlapping N–H bending and C═C stretching modes of vibration resulting from the preparation of carboxylic acid by hydrolysis of amides with warm ethanolic sodium hydroxide. Very small peaks appeared at 1573 cm^{-1} and 1398 cm^{-1} and may be due to the symmetric and antisymmetric stretching modes, respectively, of –COO–, which arose from the ionization of carboxylic acid groups in the ethanolic NaOH medium.[18] Another small peak at approximately 1434 cm^{-1} originated from the scissoring vibration of the CH_2 group.[18] The intense peak at 1331 cm^{-1} indicated formation of a S═O group due to the oxidation of cysteine disulfide cross-links present in natural hair fibers.[18] The peak at approximately 1269 cm^{-1} represented the in-plane N–H bending mode of amide II,

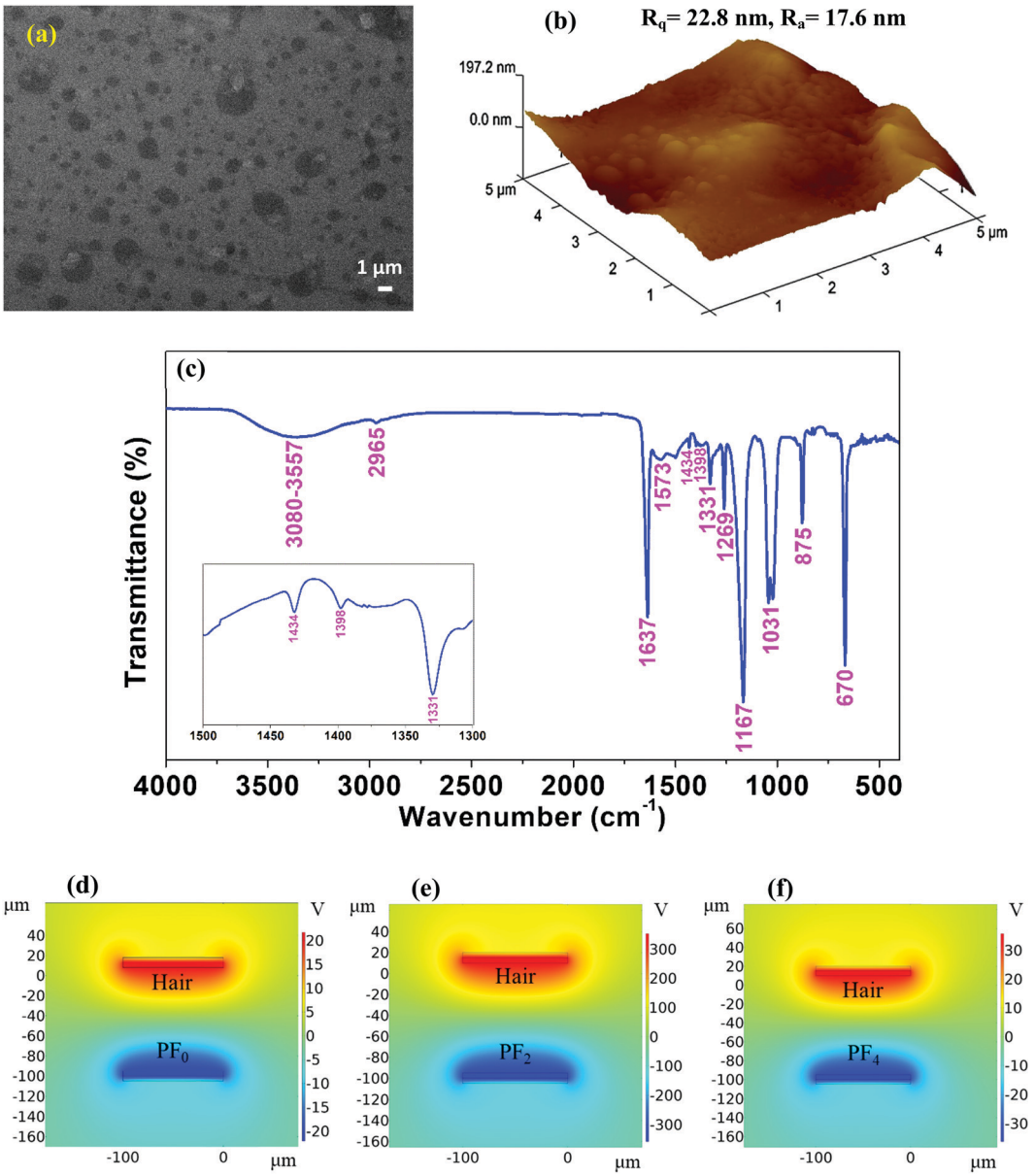

Fig. 3 (a) FESEM view of the human hair-based film. (b) AFM image (three-dimensional) of the human hair-based film. (c) FTIR spectra of the human hair-based film with an expanded spectrum view of a certain region (1300–1500 cm^{-1}) in the inset. COMSOL simulation results of the TENGs comprising the human hair based film and (d) PF_0, (e) PF_2, and (f) PF_4 film.

Table 2 EDS analysis results of the human hair-based film

Region		C K	N K	O K	Na K	Al K	S K	Ca K
Dark shaded	Weight%	44.87	14.15	26.39	3.72	3.30	6.89	0.68
	Atomic%	46.23	15.80	26.25	2.57	2.94	5.44	0.77
Light shaded	Weight%	45.99	14.57	26.59	4.35	2.68	5.24	0.58
	Atomic%	48.03	15.73	25.91	3.33	2.09	4.13	0.78

while ester C–O asymmetric stretching was indicated by the very sharp peak at 1167 cm^{-1}.[30] The sharp feature at 1031 cm^{-1} was possibly due to the presence of the C–O amide-I band.[31] The peak at 875 cm^{-1} represented the deformation of the hydrocarbons in the keratin proteins, and the peak at 670 cm^{-1} was assigned to the C–OH out-of-plane bending mode.[18] Thus, FTIR analysis suggests deformations in the chemical structure of natural hair samples after treatment in a strong base medium at a certain temperature.

To theoretically understand the output performance alteration of the α-Fe_2O_3 NP-embedded TENG, a COMSOL simulation was conducted. Fig. 3d–f demonstrates the corresponding results for the triboelectric potential distributions of TENGs based on PF_0, PF_2 and PF_4 film. As a result, the COMSOL simulations showed that the TENG with the α-Fe_2O_3 NPs embedded in PDMS films has a significantly higher triboelectric potential distribution than the TENG without α-Fe_2O_3 NPs.

TENGs held in a vertical contact-separation mode were fabricated to investigate the charge generated by the PDMS@α-Fe_2O_3

NP composite film (as the negative electrification layer) and human hair (as the positive electrification layer). Fig. 4a–f presents the effect of the α-Fe_2O_3 NP content on the output performance of the PDMS@α-Fe_2O_3 NP composite by showing the voltage, current and charge density outputs of TENGs consisting of a human hair-based film and PDMS@α-Fe_2O_3 NP composite film. As the pure PDMS film and human hair-based film surfaces approach and contact each other, electric charge transfers from the human hair-based film to the PDMS film surface because PDMS has a more negative polarity than human hair in the triboelectric series.[10,18,32] As they are separated, the electrons flow back through the outer circuit to maintain charge neutrality. In this way, upward and downward peaks are generated as the two surfaces repeat the approach/separation cycles. All devices show similar performance, even after incorporating α-Fe_2O_3 NPs, showing a similar order for polarity of the electrification layers in the devices.

Although pure α-Fe_2O_3 NPs showed relatively low levels of triboelectric output (Fig. S8, ESI†), with increase in α-Fe_2O_3 NP content in the PDMS layer, the voltage and current initially increased considerably and then decreased, as shown in Fig. 4a and b. As the NP content was increased up to 0.06 wt%, the mean peak-to-peak output voltage increased from 22.5 to 370.8 V and then decreased to 38.2 V as the NP content was increased further to 0.09 wt%. As shown in Fig. 4b and c the output current and charge density also varied in a similar way with maxima of 6 μA and 13.41 nC cm^{-2} respectively. The enhanced triboelectric output of the PDMS@α-Fe_2O_3 NP composite with a small amount of α-Fe_2O_3 NPs could be due to the

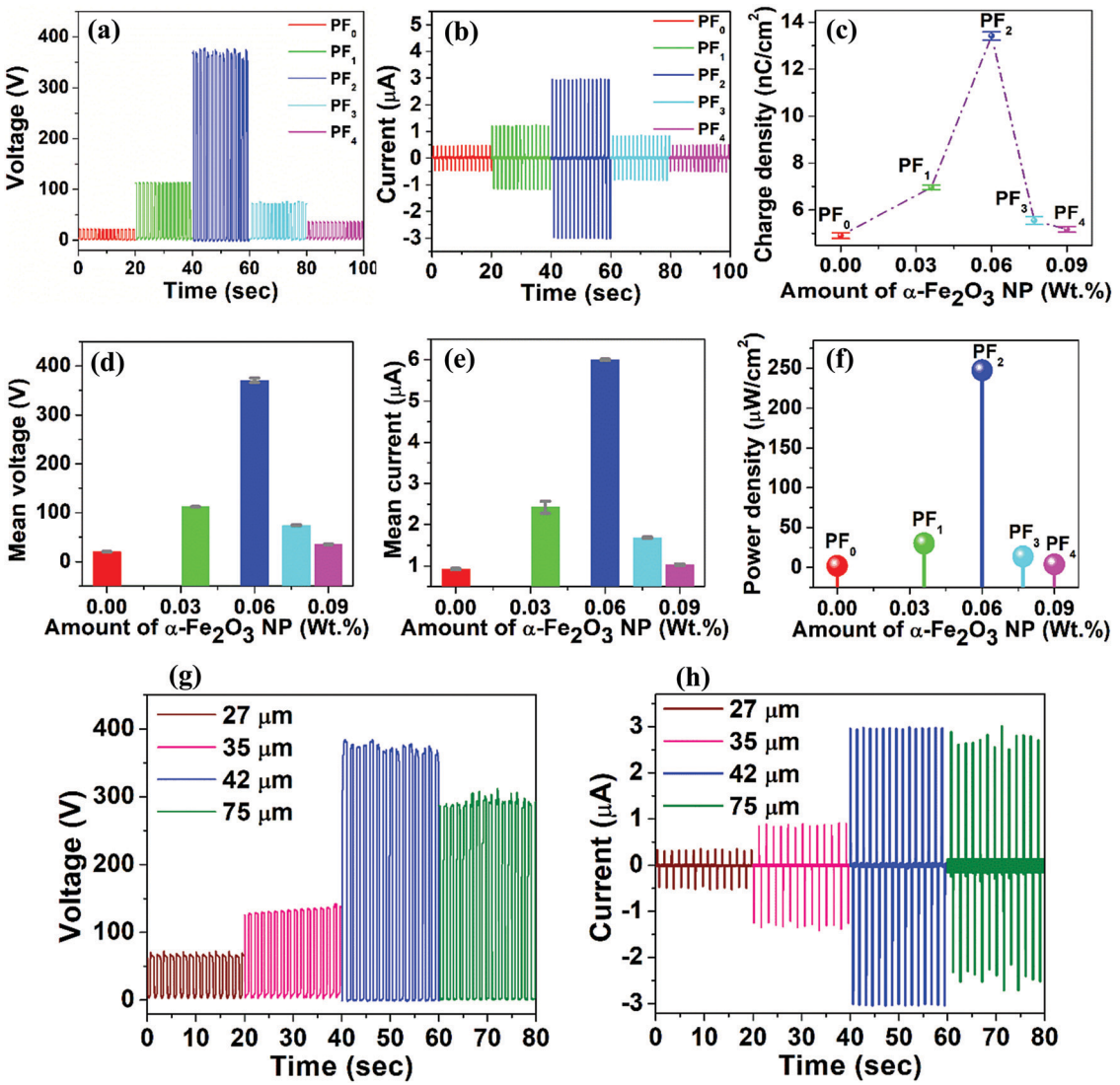

Fig. 4 (a) Voltages and (b) current outputs of TENGs comprising the PDMS@α-Fe_2O_3 NP film (as the negative electrification layer) and human hair-based film (as the positive electrification layer) as a function of α-Fe_2O_3 NP content; mean values of peak-to-peak (c) charge density, (d) voltage and (e) current outputs with standard deviations and (f) corresponding output power densities of TENGs with varying α-Fe_2O_3 NP content; (g) voltage and (h) current outputs of the PF_2 TENG comprising the PDMS@α-Fe_2O_3 NP film (as the negative electrification layer) and human hair-based film (as the positive electrification layer) with variation in the PF_2 film thickness.

enhancement in triboelectric charge density arising from efficient capture of the surface triboelectric electrons of the frictional layer and the doping effect resulting from the dielectric properties of α-Fe_2O_3.[9,20,33] However, a further increase in the α-Fe_2O_3 NP content resulted in aggregation of the NPs on the PDMS@α-Fe_2O_3 NP composite film surfaces, as shown in Fig. S2d and e (ESI†), which reduced the effective contact between the PDMS (higher electronegativity) and the human hair films; filler began to appear on the surface at higher filling contents, which ultimately resulted in degradation of the TENG performance. From PF_0 (Fig. S2b, ESI†) to PF_2 (Fig. 2a), the change in the film morphology with the appearance of nano-clefts exhibiting controlled dimensions could be another possible reason for the improvement in the TENG performance, which may have resulted from enhancement in the effective contact area between friction layers along with the improvement in surface roughness (Fig. 2c and d). With further increases in NP content, the nano-cleft began causing detachment within the friction layer, which caused degradation of the composite film properties. Therefore, the performance of the TENG was affected by both the favorable and unfavorable aspects of α-Fe_2O_3 NP incorporation, that confirms the pattern of variation depicted in COMSOL simulation results. It is mandatory to introduce an optimized amount of α-Fe_2O_3 NPs to obtain beneficial effects of NPs on the performance of the TENG device.

Variations in the mean peak-to-peak output voltage and current arising from the incorporation of α-Fe_2O_3 NPs (along with standard deviations), are demonstrated in Fig. 4d and e, and they indicate the appreciable stability of the as-developed TENG devices. Additionally, the corresponding output power densities of the PDMS@α-Fe_2O_3 NP composite and human hair-based TENG with different α-Fe_2O_3 NP loads (Fig. 4f) were calculated. The mean output power density approached a peak value of 247.2 μW cm^{-2}, which is comparable with those of other works and better than many of those reported from existing research on PDMS-based TENGs.[12,27,34–37]

Although PDMS is the second most negative triboelectric material (after PTFE)[10] in the triboelectric series, PDMS and PDMS@α-Fe_2O_3 NP composite films showed output voltages and currents higher than those seen with the use of PTFE film as a negative triboelectric layer (Fig. S9, ESI†). This may be due to the special surface morphologies of these films and the enhanced charge trapping resulting from the introduction of high dielectric α-Fe_2O_3 NPs into the PDMS matrix, which helps to improve charge transfer compared to that seen with PTFE film during the triboelectrification process.

To further optimize the performance of the TENG, the effect of film thickness on TENG performance was investigated. Additionally, the charge (Q) transferred between the electrodes is dependent on the relative dielectric constant (ε_r), surface area (S), and thickness of the dielectric film (d), as described by eqn (6). Since the transferred charge Q depends inversely on the thickness of the triboelectric film, a thinner film is expected to result in higher performance. In the present case (Fig. 4g and h), consistent with the theoretical expectation, the optimum thickness of the PDMS@α-Fe_2O_3 NP composite film that produced the highest output performance was determined to be 42 μm. Thicknesses lower than 42 μm led to nonuniformity in composite formation and inappropriate morphologies of the PDMS@α-Fe_2O_3 NP composite layers residing on the Al electrode contact; the unique charge trapping mechanism of the PDMS@α-Fe_2O_3 NP composite film was interrupted, resulting in a lower output.

To scrutinize the performance of a human hair-based positive electrification layer in the TENG device, aluminum and hair-based films of comparable thickness were tapped to PF_2, keeping all other conditions unaltered, and the polarities of the corresponding signals were studied. After tapping a material with a given friction layer, the polarity of a material determines whether it gains or loses electrons upon contact with the given friction layer; thus, we can clarify if one material has a higher affinity for acquiring negative tribo-charges relative to another. Fig. S10 (ESI†) illustrates the voltages and currents of the respective materials during 22 cycles of contact and separation. Notably, the human hair-based positive electrification layer showed much higher output voltage and current as a positive electrification layer, in comparison with aluminum film under the same conditions, which may be because the human hair-based material lost more electrons than Al during the triboelectrification process involving the lipid layer on its surface.[38] The valley surface features on the human hair-based film increased the surface roughness in comparison with that of an aluminum film (ESI,† Fig. S5a and Fig. 3b) and, since surface roughness of a triboelectric film is known to improve triboelectrification, this may have enhanced TENG performance. As depicted in Fig. S11 (ESI†), the treated hair-based film layer showed tribo-polarity similar to that of untreated human hair, even though the FTIR analysis affirms the chemical deformation of the treated hair film; there was also evidence for instability in the output voltage and current, which is due to the nonuniformity of the natural hair as a positive triboelectric layer. Thus, this film is expected to harvest natural human hair movement efficiently as a result of involuntary friction, thereby meeting users' different operation requirements if the negative part of the as-developed TENG were attached to the inner side of hair accessories such as a headband, hair clips, hair cap and normal head cap (Fig. 1).

The charge trapping properties of the α-Fe_2O_3 NPs embedded in PDMS were investigated by measuring the capacitance of the PDMS@α-Fe_2O_3 NP composite films as a function of α-Fe_2O_3 NP content and frequency (Fig. 5a). To evaluate the dielectric influence on the output of the TENG device under consideration, detailed studies of the dielectric constant in the frequency range 10^3 to 10^5 Hz were executed (Fig. 5b). There was a slight decrease in the dielectric constant with increasing frequency, which is due to the reduction of the space-charge polarization effect.[39] It is notable that the capacitance and dielectric constant of the PDMS@α-Fe_2O_3 NP composite increased significantly with increasing α-Fe_2O_3 NP amount, as shown in Fig. 5a and b and the enhancement of the dielectric constant was mainly due to the interaction between electrons in the α-Fe_2O_3 particles and the polymer matrix.[40] This result

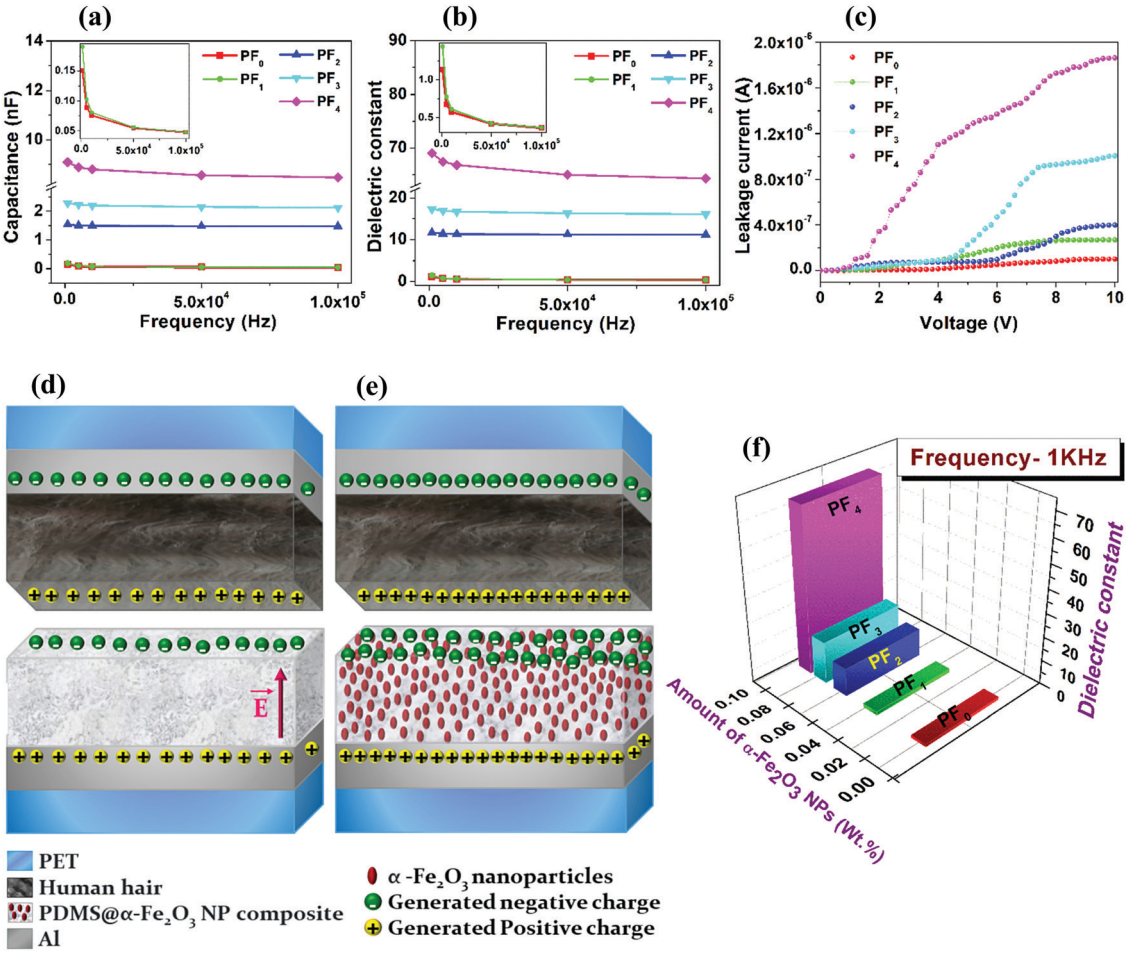

Fig. 5 (a) Capacitance and (b) dielectric constant of the PDMS@α-Fe_2O_3 NP composite films prepared with various α-Fe_2O_3 NP concentrations as a function of frequency. (c) Leakage current measured across the PDMS@α-Fe_2O_3 NP composite films prepared with various α-Fe_2O_3 NP concentrations as a function of the applied voltage. (d) Schematic of the triboelectric charge transfer process in the PDMS friction layer of the TENG. (e) Schematic of the transfer of triboelectric charges in the PDMS@α-Fe_2O_3 NP composite friction layer of the TENG. (f) Dielectric constants of PDMS@α-Fe_2O_3 NP composite films at 1 kHz frequency with different α-Fe_2O_3 NP contents.

indicated that charge trapping at the PDMS@α-Fe_2O_3 NP triboelectric layer was enhanced by the insertion of α-Fe_2O_3 NPs.[28,32,41] The addition of α-Fe_2O_3 NPs, particularly in amounts exceeding 0.077 wt%, might induce the formation of a more efficient network for charge transport in the base PDMS matrix by agglomerating nanoparticles in the film-like regions; this would improve the contact between the dielectric and metal interface of the capacitor under consideration, thus resulting in considerable enhancement of the dielectric properties of the composite film.[15,28,42–44] This improved charge trapping,[41,45,46] and the lower surface charge potential (confirmed by the KPFM results) increased the output voltage/current of the TENG.[28,32,33]

Previous studies showed that increasing amounts of embedded NPs with high dielectric constants improved TENG output because of the increasing dielectric constant of the tribo-material.[15,27,28,32] Our results show the same trends, as indicated by eqn (6). The increases in both capacitance and dielectric constant for PF_1 compared to those of PF_0 were very small, as shown in the inset of Fig. 5a and b due to the very low ratio of α-Fe_2O_3 NPs to PDMS in this composite. However, the output performance of the TENG began to degrade when the amount of α-Fe_2O_3 NPs was further increased from 0.06 wt%. The addition of more α-Fe_2O_3 NPs beyond 0.06 wt%, however, significantly increased the leakage current through the nanoparticle agglomeration, as shown in Fig. 5c. The nanoparticle agglomerates in the film-like regions of both the 0.077 and 0.09 wt% samples induced the local induction charges on the nanoparticle surfaces to flow along the film thickness direction, which may be a reasonable cause to reduce TENG performance above 0.06 wt% embedding α-Fe_2O_3 NPs.[47] Therefore, in brief, triboelectrification and dielectric constant work together to affect the performance of the TENG, and the prime composite (PF_2) illustrates the competitive balance of these influences and the effect on the output properties of the TENG.

By considering the triboelectric charge density, the charge transferred between the electrodes, the relative dielectric constants of human hair-based and PDMS@α-Fe_2O_3 NPs composite films, the distance between two induced-charge surfaces, the thicknesses of human hair-based and PDMS@α-Fe_2O_3 NPs

composite films, and the area of dielectric layer as σ_T, Q, ε_{rH}, ε_{rPF}, x, d_H, d_{PF} and S, respectively, the V–Q–x relationship of a contact-mode TENG can be derived from electrodynamics.[8,48] Since the area (S) of the metals is several orders of magnitude larger than their separation distance (($d_H + d_{PF} + x$)) in this case, it is rational to assume that the two electrodes are infinitely large. From the Gauss theorem, the electric field strength in each region is given by

Inside the human hair based film:

$$E_H = -\frac{Q}{\varepsilon_0 S \varepsilon_{rH}} \quad (1)$$

Q/S Inside the air gap:

$$E_{air} = -\frac{Q/S + \sigma_T}{\varepsilon_0} \quad (2)$$

Inside the PDMS@α-Fe_2O_3 NPs composite film:

$$E_{PF} = -\frac{Q}{\varepsilon_0 S \varepsilon_{rPF}} \quad (3)$$

Therefore, the voltage between the two electrodes is,

$$V = E_H\, d_H + E_{PF}\, d_{PF} + E_{air}\, x \quad (4)$$

Substituting eqn (1)–(3) into eqn (4),

$$V = -\frac{Q}{S\varepsilon_0}\left(\frac{d_H}{\varepsilon_{rH}} + \frac{d_{PF}}{\varepsilon_{rPF}} + x\right) + \frac{\sigma_T}{\varepsilon_0}x \quad (5)$$

Therefore, Q can be obtained from the completely released stage of the TENG devices;

$$Q = \frac{S\sigma_T}{\left(\frac{d_H}{x\varepsilon_{rH}} + \frac{d_{PF}}{x\varepsilon_{rPF}} + 1\right)} \quad (6)$$

Eqn (6) shows that the transferred charge Q increases with increasing triboelectric charge density σ_T on the dielectric surface and relative dielectric constant ε_{rPF}.

The triboelectrification mechanism can be divided into three subprocesses: generation of triboelectric charges, storage of triboelectric charges, and electrostatic induction of charges.[49] As shown in Fig. S12 (ESI†), the two film surfaces are initially not in contact, no charge transfer occurs, and hence no electric potential exists. Then, with physical contact, the PDMS@α-Fe_2O_3 NP composite film, with electron affinity higher than that of human hair, captures electrons from the human hair-based film (positive friction layer) during the triboelectrification process. Upon releasing the two substrates, the charge accumulation on the contact surfaces induces opposite charges on the rear electrodes (aluminum electrode) of both electrification layers. Thus, a potential difference is induced as a consequence of contact electrification, driving electrons *via* an external circuit from the positive electrification layer to the negative electrification layer, thus causing a negative current to flow through the external circuit. In this stage (Fig. 5d), for triboelectrification between pure PDMS film (negative friction layer) and human hair-based film (positive friction layer), a built-in electric field will be set up between the contact surface and bottom Al electrode, and this electric field is directed vertically upward. Therefore, two-electron transfer modes are generated: the first is the drift process caused by the electric field, and the other is the diffusion process caused by the concentration gradient of electrons, both resulting in the loss of triboelectric electrons due to recombination with positive charges induced on the Al electrode. This phenomenon results in the deterioration of typical TENG devices. To cope with this situation, we introduced α-Fe_2O_3 NPs embedded into the PDMS matrix to form a TENG with a PDMS@α-Fe_2O_3 NP composite film (as the negative electrification layer) and human hair-based film (as the positive electrification layer) (Fig. 5e). By taking advantage of the high theoretical capacity of the α-Fe_2O_3 nanomaterials,[50,51] an optimized amount of α-Fe_2O_3 NPs can suppress the recombination between electrons and positive charges by efficiently trapping the surface triboelectric electrons of the frictional layer; the electret doping effect resulting from the dielectric properties of the α-Fe_2O_3 NPs was reflected by the improvement in the capacitance and dielectric constant of the PDMS@α-Fe_2O_3 NP composite with an increase in the NP content (Fig. 5a, b and f). Therefore, a higher triboelectric charge density[52] and greater transferred charge Q are achieved with the TENG. In addition, human hair retaining very high positive tribopolarity will efficiently supply triboelectric electrons into the PDMS@α-Fe_2O_3 NP film, consequently strengthening the TENG performance of the device. Then, after the two films are completely released (Fig. S12d, ESI†), the output signal drops to zero. With further pressing, an instantaneous positive output signal appears due to electron flow until the induced charges become neutralized.

In order to clarify the influence of untreated hair waste on the performance of the TENGs, output voltage and current as a function of time were measured for TENGs based on the PDMS@α-Fe_2O_3 NP composite films attached to a hairband, tapped to untreated hair waste, keeping all other conditions unaltered, as shown in Fig. 6a–c. The resulting signals showed output voltage and current similar to that of the human hair based film, except the evidence for little instability in the output signals, which is due to the non-uniform stacking of the natural hair as a positive triboelectric layer. Since the TENG is based on the coupling of the triboelectric effect and electrostatic induction, its performance is closely related to the surface adsorption layers. As shown in Fig. 6d and e the performance of our TENG exhibited some degradation when PF_2 film and wet hair were tapped due to the dissipation of the built-up charges owing to the formation of a water layer on the surface of the tribolayers and the significant contribution of the water layer to the mobility of the surface charges on the hair. In spite of this reduction, our TENG still exhibited appreciably high output. To evaluate the practical applications of our TENG, a circuit consisting of a bridge rectifier and commercial capacitors was used to regulate and store the output power of the TENG. Fig. 6f shows the charging curves using a 3.3 μF capacitor, 33 μF capacitor, 47 μF capacitor and 100 μF capacitor, respectively. It can be seen that the 3.3 μF capacitor can

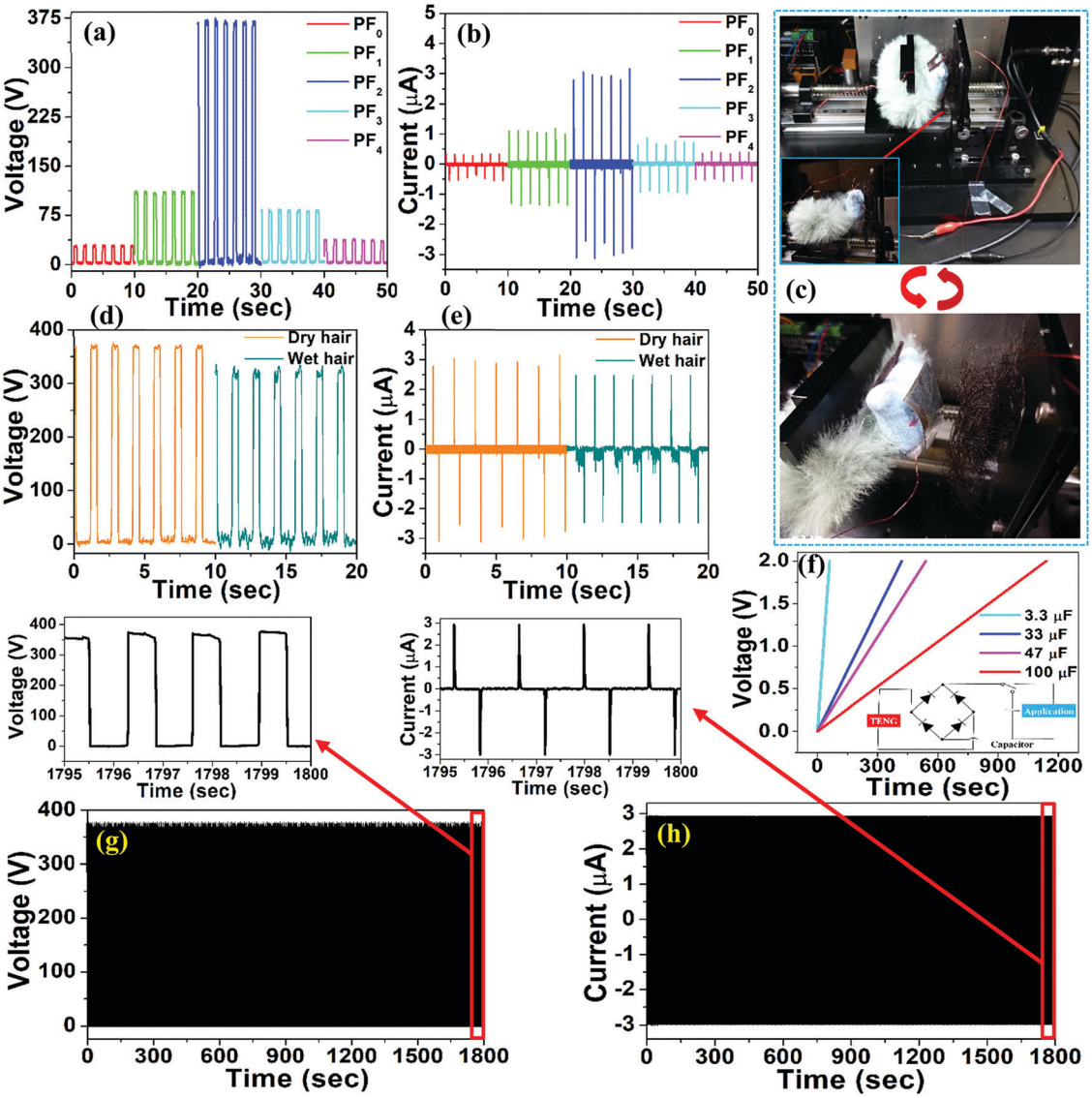

Fig. 6 (a) Voltages and (b) current outputs of TENGs comprising PDMS@α-Fe_2O_3 NP film (attached to a hairband) and natural human hair waste, as a function of α-Fe_2O_3 NP content; with the (c) photographic image of the measurement arrangement. (d) Voltage and (e) current output for dry and wet conditions of the natural human hair. (f) The charged curves using 3.3 μF, 33 μF, 47 μF and 100 μF capacitors. The output (g) voltage and (h) current stability test of the TENG comprising the PF_2 film and human hair-based film at room temperature for 30 minutes.

be charged to 2 V within 60 s, while the 33 μF capacitor can be charged to 2 V within 7 minutes, the 47 μF capacitor can be charged to 2 V within 9 minutes and the 100 μF capacitor can be charged to 2 V within 19 minutes. The mechanical stability and durability of the TENG based on our optimized PDMS@α-Fe_2O_3 NP composite film and human hair based film were measured after repeated operations over 30 minutes (Fig. 6g and h). The output voltage and current had no statistically relevant variations which indicates its outstanding reliability.

To understand the significance of this work, we have compared in Table 3 the results of this work with those of previously published studies on PDMS-based TENGs, most of which worked in a vertical contact-separation mode.[12,27,34–37] It is evident that the TENG based on the novel tribo-material combination developed in this work compares well with previous TENGs and performs better than many of them; the current TENG showed very good output resulting from the new approach to modifying PDMS with the controlled insertion of α-Fe_2O_3 NPs. This is a convenient and cost-effective method and the use of human hair as a positive tribo-material offers a solid basis for biowaste management, with which novel technologies can be coupled.

Conclusions

In summary, we have demonstrated facile cost-effective chemical methods for synthesizing α-Fe_2O_3 nanoparticles and embedding them in a PDMS matrix to produce a PDMS@α-Fe_2O_3 NP composite serving as a superior negative electrification layer; this was accompanied by processing hair into a

Table 3 Comparison of the output performance of the TENG prepared in this work with those of similar tribo-materials reported by other researchers

Positive Tribo-material	Negative Tribo- material	Peak-to-peak voltage (V)	Output power density (μW cm^{-2})	Ref.
PET	Pyramid patterned arrays of PDMS	18	2.34	12
ZnO NRAs	PDMS	5.34	0.24	34
Aluminum	TiO_{2-x} NPs embedded PDMS	180	163	35
Aluminum	Surface-embossed PDMS achieved *via* control of ZnO nano-flakes (NF)	130	188.5	36
Cu	Micro-frustum-array-structured PDMS film and (P(VDF-TrFE)) nanofibers	23	2.66	37
PET	PDMS-FDTS	125	73	27
Human hair	PDMS@α-Fe_2O_3 NP composite	370.8	247.2	This work

suitable form with appreciable uniformity for use as a positive electrification layer in a TENG. Structural, morphological, and compositional analyses using XRD, FESEM, AFM, EDS, and FTIR spectroscopy confirmed the successful syntheses of the above samples. As the α-Fe_2O_3 NP content in the negative electrification layer was increased up to 0.06 wt%, the output voltage increased from 22.5 to 370.8 V, and then it decreased to 38.2 V as the NP content increased further up to 0.09 wt%. The α-Fe_2O_3 NPs improved the TENG performance by combining the effects of a successfully developed special film morphology exhibiting nano-clefts of controlled dimensions with the electret doping effect observed with small amounts of incorporation; however, the NPs detrimentally affected the TENG performance at high incorporation levels because they aggregated and caused detachment within the electrification layer. In addition, by taking advantage of the intense triboelectrification effect of human hair, the hair was processed to develop a superior positive electrification layer for TENGs and avert environmental problems caused by slowly degrading human hair waste material. Therefore, the PDMS@α-Fe_2O_3 NP composite and human hair-based TENG provide a promising high-level power supply for wearable electronics and self-powered smart portable electronics; the TENG harvests mechanical energy while expanding human hair utilization, constituting a promising approach toward the recycling bioeconomy that will play an important role in avoiding climate emergencies.

Experimental section

Materials

PDMS (SYLGARD 184, DOW CORNING, USA) was purchased for fabricating elastomeric nanocomposites. Iron(III) chloride hexahydrate (98.0–102%) (Sigma Aldrich) and ammonium hydroxide solution (~25% NH_3 basis) (Honeywell Fluka) were purchased for hydrothermal synthesis of α-Fe_2O_3 NPs, which was selected as the incorporating material. Ethanol (Honeywell, ≥99.8%) and NaOH (SHIMAKYU'S PURE CHEMICALS) were used without further purification.

Fabrication of the unmodified PDMS film-based negative electrification layer

The PDMS solution was prepared by mixing the Sylgard 184 elastomer with the curing agent in a 10 : 1 proportion with magnetic stirring. After that, the as-prepared solution was spin-coated (at 2500 rpm for 60 s) onto Al-coated flexible PET and cured at 80 °C for 2 hours, and this sample was subsequently referred to as PF_0.

Preparation of α-Fe_2O_3 nanoparticles

α-Fe_2O_3 nanoparticles were prepared by the hydrothermal method. In the first step, 156 mg of $FeCl_3 \cdot 6H_2O$ was sonicated in 40 ml DI water in a bath sonicator for 15 minutes to form a homogeneous solution. Then, 5.6 ml of 25% ammonia solution was added slowly (dropwise) for 30 minutes with constant stirring. Immediately, the mixed solution was transferred into a Teflon-lined steel autoclave (50 ml), sealed and heated at 180 °C for 12 hours, after which it was naturally cooled to room temperature. The product collected from the autoclave was then centrifuged and washed with deionized water and ethanol (1 : 1) several times to neutralize the pH, and the material was dried in air at 60 °C for 12 hours to obtain rod-like α-Fe_2O_3 nanoparticles.

Fabrication of a PDMS@α-Fe_2O_3 NP film-based negative electrification layer

Fig. S1b (ESI†) shows a schematic diagram of the process of fabricating the PDMS@α-Fe_2O_3 NP composite film (negative electrification layer) over a flexible PET substrate with Al as the electrode. In this experiment, the PDMS solution (Sylgard 184) contained both the elastomer (PDMS) and the curing agent (elastomer was thoroughly mixed with the curing agent at a weight ratio of 10 : 1). To prepare the PDMS@α-Fe_2O_3 NP composite film, the as-prepared α-Fe_2O_3 NPs dispersed in DI water were first mixed into PDMS by magnetic stirring for approximately 3–4 hours until there were no bubbles in the liquid. For the comparative study, a PDMS@α-Fe_2O_3 NP composite film was prepared with four different weight percentages of α-Fe_2O_3 NPs. These samples are hereafter referred to as PF_1 (0.036 wt% α-Fe_2O_3 NPs), PF_2 (0.06 wt% α-Fe_2O_3 NPs), PF_3 (0.077 wt% α-Fe_2O_3 NPs) and PF_4 (0.09 wt% α-Fe_2O_3 NPs). The negative electrification layer of the TENGs was prepared by spin-coating (at 1200–2100 rpm for 60 s) the homogeneous solutions described above onto a 3 × 3 cm^2 A1 covered flexible PET substrate whose surface was cleaned with a N_2 gun before spin coating. The negative electrification layers were then cured at 80 °C for 2 hours. For the PDMS@α-Fe_2O_3 NP composite film,

additional curing at 105 °C for 2–3.5 hours was required to remove the DI water. This selective drying process is very important to control the film morphology with irregular nano-clefts.

Fabrication of a human hair film-based positive electrification layer

Scalp hair samples were collected from 20–30 year-old women (Asian). First, 1.5 gm of hair was intensively washed with ethanol and DI water, then dried at 60 °C for 30 minutes. Then, this clean hair was submerged in 40 ml of 1.5 M ethanolic NaOH solution, sealed and heated at 60 °C for 12 hours. After cooling naturally to room temperature, this processed hair mass was washed through centrifugation with ethanol, and then the resulting hair mass was dissolved in an equal amount of DI water with ultrasonication to obtain a homogeneous solution. As shown in Fig. S1a (ESI†), to prepare the positive side of the TENGs, a 16.7 μm thick film was deposited by spin-coating (at 1500 rpm for 40 s) the as-prepared homogeneous solution onto an A1-covered flexible PET substrate surface that had been cleaned by a N_2 gun before spin coating, and then the sample was dried at 60 °C for 5 hours. The total contact area of the TENG was 3 × 3 cm^2. The TENGs (Fig. S1c, ESI†) were operated with vertical contact-separation modes.

This experiment was performed in compliance with the institute's rules on the use of human subjects and the hair waste samples were collected from some Asian women with their consent.

Material characterization and electrical measurements

The crystalline phase and the surface charge potential of the PDMS@α-Fe_2O_3 NP composite films were systematically analyzed by X-ray diffraction (X-ray Diffraction for Thin Film Advanced Analysis and X-ray Powder Diffractometer equipped with a Cu Kα source) and Kelvin probe force microscopy (KPFM, Dimension-3100 Multimode, Digital Instruments). The surface morphologies and elemental analyses of the α-Fe_2O_3 NPs, PDMS@α-Fe_2O_3 NP composite films with different wt% α-Fe_2O_3 NPs and human hair-based film were investigated using FE-SEM combined with energy-dispersive spectroscopy (EDS) (FE-SEM, JEOL JSM-7500F) and AFM (Innova B067, Bruker Corp. USA). The chemical bonding of the α-Fe_2O_3 NPs, PDMS@α-Fe_2O_3 NPs composite films with different weight% of α-Fe_2O_3 NPs and human hair-based film was investigated using a Howard Infrared Spectrometer-Microscope with an ATR microscopy accessory. The thickness of the PDMS@α-Fe_2O_3 NP composite films and human hair-based film was obtained by an Alpha stepper (DektakXT, Bruker). All electrical properties of the TENG were measured by using a Keithley 6514 programmable electrometer and a low-noise current preamplifier (Stanford Research System Model SR570). The capacitances and leakage currents of the PDMS film and PDMS@α-Fe_2O_3 NP composite films were measured using an Agilent B1500A semiconductor device parameter analyzer at room temperature.

Author contributions

I. C. and C.-S. L. conceived the idea and designed the work. I. C. prepared the samples and measured the devices. I. C., S.-N. L., M.-C. W., J. M. W and C.-S. L. were involved in the discussion and characterization. I. C., H.-Y. L and S.-N. L. interpreted the experimental results and conducted the theoretical mechanisms. I. C. prepared the manuscript and S.-N. L., M.-C. W., C. L., J. M. W., C.-S. L. revised it.

Conflicts of interest

There is no conflict of interest to declare.

Acknowledgements

The authors acknowledge the financial support provided by the Ministry of Science and Technology, Taiwan under project numbers of MOST 109-2221-E-182-013-MY3, MOST 110-2622-8-182-001-TS1 and MOST 110-2119-M-492-002-MBK, and Chang Gung Memorial Hospital Research Project under grant numbers of CMRPD2K0171 and CORPD2J0072.

References

1 J. M. Wu, Y. H. Lin and B.-Z. Yang, *Nano Energy*, 2016, **22**, 468–474.
2 S.-N. Lai, C.-K. Chang, C.-S. Yang, C.-W. Su, C.-M. Leu, Y.-H. Chu, P.-W. Sha and J. M. Wu, *Nano Energy*, 2019, **60**, 715–723.
3 F. R. Fan, Z. Q. Tian and Z. L. Wang, *Nano Energy*, 2012, **1**, 328–334.
4 Z. L. Wang, *Faraday Discuss.*, 2014, **176**, 447–458.
5 S. Niu and Z. L. Wang, *Nano Energy*, 2015, **14**, 161–192.
6 H. Kang, H. Kim, S. Kim, H. J. Shin, S. Cheon, J.-H. Huh, D. Y. Lee, S. Lee, S.-W. Kim and J. H. Cho, *Adv. Funct. Mater.*, 2016, **26**, 7717–7724.
7 J. Chun, B. U. Ye, J. W. Lee, D. Choi, C.-Y. Kang, S.-W. Kim, Z. L. Wang and J. M. Baik, *Nat. Commun.*, 2016, **7**, 12985.
8 J. M. Wu, C. K. Chang and Y. T. Chang, *Nano Energy*, 2016, **19**, 39–47.
9 J.-S. Im and I.-K. Park, *ACS Appl. Mater. Interfaces*, 2018, **10**, 25660–25665.
10 J. W. Lee, B. U. Ye and J. M. Baik, *APL Mater.*, 2017, **5**, 073802.
11 J. Xiong, P. Cui, X. Chen, J. Wang, K. Parid, M.-F. Lin and P. S. Lee, *Nat. Commun.*, 2018, **9**, 4280.
12 F.-R. Fan, L. Lin, G. Zhu, W. Wu, R. Zhang and Z. L. Wang, *Nano Lett.*, 2012, **12**, 3109–3114.
13 C. K. Jeong, K. M. Baek, S. Niu, T. W. Nam, Y. H. Hur, D. Y. Park, G.-T. Hwang, M. Byun, Z. L. Wang, Y. S. Jung and K. J. Lee, *Nano Lett.*, 2014, **14**, 7031–7038.
14 X.-S. Zhang, M.-D. Han, R.-X. Wang, B. Meng, F.-Y. Zhu, X.-M. Sun, W. Hu, W. Wang, Z.-H. Li and H.-X. Zhang, *Nano Energy*, 2014, **4**, 123–131.

15 J. Chen, H. Guo, X. He, G. Liu, Y. Xi, H. Shi and C. Hu, *ACS Appl. Mater. Interfaces*, 2016, **8**, 736–744.
16 D. Kim, S.-J. Park, S.-B. Jeon, M.-L. Seol and Y.-K. Choi, *Adv. Electron. Mater.*, 2016, **2**, 1500331.
17 J.-G. Sun, T. N. Yang, I.-S. Kuo, J.-M. Wu, C.-Y. Wang and L. J. Chen, *Nano Energy*, 2017, **32**, 180–186.
18 E. N. Jayaweera, K. R. Wijewardhana, T. K. Ekanayaka, A. Shahzad and J.-K. Song, *ACS Sustainable Chem. Eng.*, 2018, **6**, 6321–6327.
19 C. T. Cherian, J. Sundaramurthy, M. Kalaivani, P. Ragupathy, P. S. Kumar, V. Thavasi, M. V. Reddy, C. H. Sow, S. G. Mhaisalkar, S. Ramakrishna and B. V. R. Chowdari, *J. Mater. Chem.*, 2012, **22**, 12198.
20 G. Binitha, M. S. Soumya, A. A. Madhavan, P. Praveen, A. Balakrishnan, K. R. V. Subramanian, M. V. Reddy, S. V. Nair, A. S. Nair and N. Sivakumar, *J. Mater. Chem. A*, 2013, **1**, 11698.
21 N. V. Long, T. Teranishi, Y. Yang, C. M. Thi, Y. Cao and M. Nogami, *Int. J. Miner., Metall. Mater.*, 2015, **1**, 119.
22 J. Sundaramurthy, P. S. Kumar, M. Kalaivani, V. Thavasi, S. G. Mhaisalkar and S. Ramakrishna, *RSC Adv.*, 2012, **2**, 8201–8208.
23 Y. Li, Y. Lu, H. Hong, Y. Chen, X. Ma, L. Guo, Z. Wang, J. Chen, M. Zhu, J. Ni, H. Gu, J. Lu and J. Y. Ying, *Chem. Commun.*, 2011, **47**, 6320–6322.
24 N. Stafie, D. F. Stamatialis and M. Wessling, *Sep. Purif. Technol.*, 2005, **45**, 220–231.
25 D. M. S. N. Dissanayake, M. M. M. G. P. G. Mantilaka, T. C. Palihawadana, G. T. D. Chandrakumara, R. T. D. Silva, H. M. T. G. A. Pitawala, K. M. N. D. Silva and G. A. J. Amaratunga, *RSC Adv.*, 2019, **9**, 21249.
26 J.-Y. Park, H. Y. Chae, C.-H. Chung, S. J. Sim, J. Park, H. H. Lee and P. J. Yoo, *Soft Matter*, 2010, **6**, 677–684.
27 G.-Z. Li, G.-G. Wang, Y.-W. Cai, N. Sun, F. Li, H.-L. Zhou, H.-X. Zhao, X.-N. Zhang, J.-C. Han and Y. Yang, *Nano Energy*, 2020, **75**, 104918.
28 S. Cheon, H. Kang, H. Kim, Y. Son, J. Y. Lee, H.-J. Shin, S.-W. Kim and J. H. Cho, *Adv. Funct. Mater.*, 2018, **28**, 1703778.
29 M. A. Mujeeb and K. M. Zafar, *Int. J. Environ. Sci. Technol.*, 2017, **6**, 2036–2040.
30 P. Garidel and H. Schott, *BioProcess Int.*, 2006, 40–46.
31 M. A. Mujeeb and M. K. M. Zafar, *IJIRSET*, 2017, **6**, 9327–9332.
32 V. Harnchana, H. V. Ngoc, W. He, A. Rasheed, H. Park, V. Amornkitbamrung and D. J. Kang, *ACS Appl. Mater. Interfaces*, 2018, **10**, 25263–25272.
33 R. Wen, J. Guo, A. Yu, J. Zhai and Z. L. Wang, *Adv. Funct. Mater.*, 2019, **29**, 1807655.
34 Y. H. Ko, G. Nagaraju, S. H. Lee and J. S. Yu, *ACS Appl. Mater. Interfaces*, 2014, **6**, 6631–6637.
35 H.-W. Park, N. D. Huynh, W. Kim, H. J. Hwang, H. Hong, K. H. Choi, A. Song, K.-B. Chung and D. Choi, *Micromachines*, 2018, **9**, 407.
36 D. Choi, S. Yang, C. Lee, W. Kim, J. Kim and J. Hong, *ACS Appl. Mater. Interfaces*, 2018, **10**, 33221–33229.
37 J. Yu, X. Hou, M. Cui, S. Shi, J. He, Y. Sun, C. Wang and X. Chou, *Sci. China. Mater.*, 2019, **62**, 1423–1432.
38 D. W. Kim, S.-W. Kim and U. Jeong, *Adv. Mater.*, 2018, **30**, 1804949.
39 C. Rayssi, S. E. Kossi, J. Dhahri and K. Khirouni, *RSC Adv.*, 2018, **8**, 17139–17150.
40 K. Hayashida, *RSC Adv.*, 2016, **6**, 64871–64878.
41 S. R. Pendlebury, X. Wang, F. L. Formal, M. Cornuz, A. Kafizas, S. D. Tilley, M. Grätzel and J. R. Durrant, *J. Am. Chem. Soc.*, 2014, **136**, 9854–9857.
42 V. Ganesh, S. Pitchumani and V. Lakshminarayanan, *J. Power Sources*, 2006, **158**, 1523–1532.
43 M. V. Reddy, G. V. S. Rao and B. V. R. Chowdari, *Chem. Rev.*, 2013, **113**, 5364–5457.
44 Z. Yu, L. Tetard, L. Zhai and J. Thomas, *Energy Environ. Sci.*, 2015, **8**, 702–730.
45 W. Y. Sohn, M. Inaba, T. Tokubuchi, J. E. Thorne, D. Wang and K. Katayama, *J. Phys. Chem. C*, 2019, **123**, 6693–6700.
46 W. Seung, H.-J. Yoon, T. Y. Kim, H. Ryu, J. Kim, J.-H. Lee, J. H. Lee, S. Kim, Y. K. Park, Y. J. Park and S.-W. Kim, *Adv. Energy Mater.*, 2017, **7**, 1600988.
47 H. J. Hwang, J. S. Kim, W. Kim, H. Park, D. Bhatia, E. Jee, Y. S. Chung, D. H. Kim and D. Choi, *Adv. Energy Mater.*, 2019, **9**, 1803786.
48 S. Niu, S. Wang, L. Lin, Y. Liu, Y. S. Zhou, Y. Hu and Z. L. Wang, *Energy Environ. Sci.*, 2013, **6**, 3576–3583.
49 V. Vivekananthan, A. Chandrasekhar, N. R. Alluri, Y. Purusothaman and S.-J. Kim, *Nanoscale Adv.*, 2020, **2**, 746–754.
50 X. Zheng and J. Li, *Ionics*, 2014, **20**, 1651–1663.
51 M. Chen, E. Zhao, Q. Yan, Z. Hu, X. Xiao and D. Chen, *Sci. Rep.*, 2016, **6**, 29381.
52 A. Li, Y. Zi, H. Guo, Z. L. Wang and F. M. Fernández, *Nat. Nanotechnol.*, 2017, **12**, 481–487.

